Title: Imaging interlayer exciton superfluidity in a 2D semiconductor heterostructure

Authors: Jacob Cutshall[1†], Fateme Mahdikhany[1,2†], Anna Roche[1], Daniel N. Shanks[1], Michael R. Koehler[3], David G. Mandrus[4-6], Takashi Taniguchi[7], Kenji Watanabe[8], Qizhong Zhu[9,10], Brian J. LeRoy[1], John R. Schaibley[1*]

Affiliations:

[1]Department of Physics, University of Arizona, Tucson, Arizona 85721, USA

[2]McCormick School of Engineering, Department of Materials Science and Engineering, Northwestern University, Evanston, IL 60208

[3]IAMM Diffraction Facility, Institute for Advanced Materials and Manufacturing, University of Tennessee, Knoxville, TN 37920

[4]Department of Materials Science and Engineering, University of Tennessee, Knoxville, Tennessee 37996, USA

[5]Materials Science and Technology Division, Oak Ridge National Laboratory, Oak Ridge, Tennessee 37831, USA

[6]Department of Physics and Astronomy, University of Tennessee, Knoxville, Tennessee 37996, USA

[7]Research Center for Materials Nanoarchitectonics, National Institute for Materials Science, 1-1 Namiki, Tsukuba 305-0044, Japan

[8]Research Center for Electronic and Optical Materials, National Institute for Materials Science, 1-1 Namiki, Tsukuba 305-0044, Japan

[9]Guangdong Basic Research Center of Excellence for Structure and Fundamental Interactions of Matter, Guangdong Provincial Key Laboratory of Quantum Engineering and Quantum Materials, School of Physics, South China Normal University, Guangzhou 510006, China

[10]Guangdong-Hong Kong Joint Laboratory of Quantum Matter, Frontier Research Institute for Physics, South China Normal University, Guangzhou 510006, China

[†]These authors contributed equally to this work.
[*]**Corresponding Author:** John Schaibley, johnschaibley@arizona.edu

Abstract:

Excitons, which are Coulomb bound electron-hole pairs, are composite bosons and thus at low temperature can form a superfluid state with a single well-defined amplitude and phase. We directly image this macroscopic exciton superfluid state in an hBN-separated $MoSe_2$-WSe_2 heterostructure. At high density, we identify quasi-long-range order over the entire active area of our sample, through spatially resolved coherence measurements. By varying the exciton density and sample temperature, we map out the phase diagram of the superfluid. We observe the superfluid phase persisting to a temperature of 15 K, which is in excellent agreement with theoretical predictions. This works paves the way to realizing on chip superfluid structures capable of studying fundamental physical behaviors as well as quantum devices that utilize superfluidity.

Introduction

Bosons, unlike fermions, can all occupy the same quantum mechanical state. At low temperatures, bosons become degenerate forming a macroscopic wavefunction. While two-dimensional systems cannot have true long-range order, at sufficiently high densities, bosons in 2D have been predicted to undergo a Berezinskii-Kosterlitz-Thouless phase transition to a superfluid state (*1, 2*). Van der Waals heterostructures are an exciting platform for the study of these correlated states due to their wide tunability through the choice of materials and coupling between layers (*3*). In certain bilayer semiconductor systems, interlayer excitons (IX) can form, which are composite bosons, composed of Coulomb bound electrons and holes in opposite layers (*4*). $MoSe_2$-WSe_2 semiconductor heterostructures host interlayer excitons (IX's) due to their type-II band alignment (*5*). These IXs have been shown to host long lived valley polarization (*6*), highly tunable energies (*7*), novel moiré physics (*8-11*), and tunable quantum dots (*12, 13*). The introduction of an hBN spacer between the $MoSe_2$ and WSe_2 layers suppresses the moiré potential and extends the lifetime of these IXs by orders of magnitude, allowing for long range IX transport and reports of increased temporal coherence (*14-16*), correlated insulating states (*17*), an correlated fluids (*18*). Pioneering theoretical work by Fogler, Butov and Novoselov (*19*), which predicted the existence of high temperature IX superfluidity in an hBN separated homobilayer, has led to intense theoretical interest in IX superfluidity (*20-22*). While evidence of degenerate exciton states have been reported in some 2D materials (*23-25*), and superfluidity in graphene (*26*), experimental demonstrations of IX superfluidity in 2D semiconductors are lacking.

Results

In this work, we image IX superfluidity in an hBN-encapsulated $MoSe_2$-bilayer hBN-WSe_2 heterostructure. The geometry of the sample is shown in Fig. 1A. One region is constructed with the $MoSe_2$ directly contacting (denoted DC) the WSe_2 with a near 0° twist angle. In the other region, a bilayer hBN spacer (denoted hBN), was inserted between the $MoSe_2$ and WSe_2 layers to suppress the moiré potential and extend the IX lifetime to 1.9 μs (fig. S1). Here, we study the IXs that were optically excited in the hBN separated region. Specifically, we performed spatial coherence measurements on the photoluminescence (PL) emitted from the hBN separated region as a measure of the quasi-long-range spatial coherence of the IX phase.

A depiction of the experiment is shown in Fig. 1B. The sample was held in an optical cryostat at temperatures down to 1.6 K. An integrated high NA objective lens was used to excite the sample with a 720 nm laser and to collect the PL emitted by the IXs. The collected PL was sent through a Mach-Zehnder interferometer. Dove prisms were introduced in the interferometer arms so that the PL image in one arm was rotated 180° from the other to allow for non-local spatial coherence measurements (Fig. 1C). A delay stage was used to control the time delay between the arms. The PL in each arm was recombined and then imaged onto a camera resulting in the interferogram shown in Fig. 1C.

The resulting interferogram (Fig. 1C) is given by (*27, 28*):

$$I_t(\vec{r}) = I_1(\vec{r}) + I_2(\vec{r}) + 2\sqrt{I_1(\vec{r}) I_2(\vec{r})}\, g^{(1)}(\vec{r}, t). \tag{1}$$

Where $I_t(\vec{r})$ is the measured PL intensity on the camera at position $\vec{r}$, I_1 and I_2 are intensities from Arm 1 and Arm 2 of the interferometer respectively (Fig. 1C), and $g^{(1)}(\vec{r}, t)$ is the first order coherence function at position $\vec{r}$ and time delay t. For short time scans near zero time delay, t_0 ($<$ 20 fs) there is no appreciable temporal decay in $g^{(1)}$ (fig. S2A). Therefore the temporal portion of the coherence function oscillates with time delay as $g^{(1)}(\vec{r},t)$= $g^{(1)}(\vec{r})\cos\left(\frac{2\pi}{\lambda}c(t-t_0)+\vec{q}\cdot\vec{r}+\phi(\vec{r})\right)$ where $\vec{q}=\frac{2\pi\alpha}{\lambda}$ is the spatial frequency of the fringes associated with a tilt angle α in one of the arms and ϕ is the phase of the wavefunction. This allows both the spatial dependence of the amplitude and phase to be extracted. We define the interference contrast at a given time delay as $\mathrm{S}(\vec{r},t)$:

$$S(\vec{r},t)=\frac{I_t(\vec{r})-I_1(\vec{r})-I_2(\vec{r})}{2\sqrt{I_1(\vec{r})I_2(\vec{r})}}=g^{(1)}(\vec{r})\,cos\left(\frac{2\pi}{\lambda}c(t-t_0)+\vec{q}\cdot\vec{r}+\phi(\vec{r})\right). \tag{2}$$

The observed interference contrast (from the interferogram shown in Fig. 1C) is shown in Fig. 2A. A mask is applied to show only the overlap region of the interfered PL. A series of delay stage scans were taken over 13 fs with 0.5 fs steps centered around t_0. Figure 2B shows the interference contrast for a single point (green dot in Fig. 2A) as a function of time delay. The amplitude of the interference contrast for each point ($\vec{r}$) is used to extract the spatial coherence function $g^{(1)}(\vec{r})$ (supplementary text S1).

Figure 2C shows the amplitude of the first order spatial coherence function for the hBN separated emission at 1.6 K and 150 µW excitation power. The two arms of the interferometer are rotated 180° relative to each other about the center of the sample region. The resulting interferogram is therefore measuring the PL emitted from point $\overrightarrow{r'}$ from the sample interfering with PL from point $-\overrightarrow{r'}$, where $\overrightarrow{r'}$ is measured from the center of the sample region. As expected, a small central spot of high coherence is observed (corresponding to $\overrightarrow{r'}=-\overrightarrow{r'}=0$) with a diameter on the order of the resolution (point spread function) of the objective (~0.5 µm) (*29*), while a lower but finite degree of coherence is present over the entire overlap region of the Arm 1 and Arm 2 PL. The 0.5 µm diameter central spot persists for all powers and temperatures and is a result of the spatial coherence of the same point in space with itself.

BKT theory predicts that when a system of IXs with a density n_{IX} cools below a critical temperature given by $T_{BKT}\approx 1.3\frac{\hbar^2 n_{IX}}{k_B m_{IX}}$ (*19, 30*), they will undergo a phase transition to a macroscopic superfluid state (where, $\hbar$ is the reduced Planck's constant, k_B is Boltzmann's constant, and m_{IX} is the IX mass). The transition temperature of this state increases linearly with increasing density and is categorized by quasi-long-range coherence with a near uniform phase. In the experiment, the IX density is controlled by varying the excitation laser power (supplementary text S3). Figure 3A-C shows the excitation power dependence of the interference fringes at 15 K. At low excitation power (Fig. 3A), there are only interference fringes at the center of the image due to the self-coherence of the central spot. There is no long-range coherence as the IXs are in the gas phase. As the excitation power is increased the interference fringes spread over the entire overlap region demonstrating the emergence of quasi-long-range coherence in the system and the transition to a superfluid state. Figures 3D-F show the amplitude of the spatially resolved first order coherence for the fringes shown in A-C. As the excitation power is increased, the spatial extent of the (blue) long range coherence increases and becomes nearly uniform across the overlap region (Fig. 3F). Figure 3G-I shows the phase for each power, showing that the coherence fringes maintain a uniform phase over the entire hBN overlap region (supplementary text S2). This is contrasted with coherence measurements performed on the DC region (fig. S3), which show a strong central $g^{(1)}$ spot in agreement with a previous work (*28*). In addition, the DC region shows clear dislocations in the fringe contrast and a non-uniform amplitude and phase.

To understand the temperature and density dependence of the IX coherence, a series of measurements was taken for excitation powers from 5 µW - 300 µW at temperatures of 1.6 K, 5 K, 10 K, 15 K, and 20 K. The temperature dependence of the interference fringes in the hBN separated region for 10 µW excitation power is shown in Fig. 4A-D. For this fixed exciton density, the spatial extent of the interference fringes abruptly decreases between 5 K and 10 K, showing the predicted loss of the coherent superfluid state as the temperature is increased. We note that the results were reproducible over multiple measurements and cooldowns.

Due to the unknown interlayer carrier transfer rate in a bilayer hBN separated heterostructure, estimation of the IX density for the hBN region is difficult. However, extensive research has been done on direct contact heterostructures (*31, 32*), allowing for an estimation of density in the DC region. Since the interlayer carrier transfer rate in direct contact heterostructures is much faster than the intralayer decay rate, the exciton density is determined by the lifetime of IXs. Using the known lifetimes of IXs in each region at low power, and the measured intensities of each region's PL, the relative densities can be estimated, and the density of the hBN region can be resolved. For each excitation power, the IX density was calculated using the measured PL intensity and lifetime (supplementary text S3 and fig. S6).

To quantify the density and temperature dependence of the quasi-long-range spatial coherence, the first order coherence function was radially averaged 1.2 μm from the central spot (white dashed line in Figs. 3D-F) corresponding to the coherence between all locations 2.4 μm apart from each other on the sample. This location was selected as it is well away from the central spot but the PL signal remains nearly constant (figs. S4 and S5). This average value is plotted for each power (density) and temperature in the phase diagram (Fig. 4E). In the hBN separated region, an abrupt transition temperature is observed below which quasi-long-range coherence is observed. This transition agrees very well with the predicted BKT transition shown by the dashed white line. We note that the phase diagram in the DC region is featureless (see fig. S7) indicating the absence of a transition to the superfluid state. We note that lower value of $g^{(1)}$ measured on the hBN separated region is dominated by interferometer noise arising from the longer integration time required to obtain sufficient signal to noise (see supplementary text S4 and fig S8).

A feature of a superfluid state is algebraic scaling in both temporal coherence and spatial coherence (*33*). Fig. S9A shows a power law fit of the form $\mathrm{g(u) = Au^b}$ to the radially averaged spatial coherence away from the center and the temporal coherence at 1.6 K for an IX density of ~2 $\times 10^{12}\ \mathrm{cm}^{-2}$. The higher temperature trace in fig. S9B shows a faster decay, which is expected as the IXs is no longer in a superfluid state. Furthermore, fig. S10 shows that there is substantial narrowing of the IX PL emission with increasing excitation laser power.

Discussion

Previous studies of correlated excitonic fluids could not perform direct optical measurements like the methods used here due to the limited IX PL signal emitted by > 1 nm thick hBN separated $MoSe_2$-WSe_2 heterostructures (*18, 23*). This work presents the first direct observation of the quasi-long-range spatial coherence present in an IX superfluid, persisting to temperatures of 15 K. Here, we observe clear onsets of spatial coherence at low temperature and high density in excellent quantitative agreement with BKT theory (*19*).

Beyond this work, we foresee that IX superfluids will be of immense interest in qubit and transistor design, where superfluid IXs can enable lossless IX transport carrying valleytronic information (*34*), and can mimic the physical behaviors of superconducting circuits (*35, 36*). The direct observation of IX superfluidity presented here allows for the construction of on-chip, experimentally accessible temperature qubits, and IX superfluid circuitry using 2D semiconductors.

Materials and Methods

Sample Fabrication

All 2D material layers were isolated by exfoliation onto Si/SiO_2 wafers using scotch tape. $MoSe_2$ and WSe_2 monolayers were selected with atomic force microscopy (AFM) and optical contrast. Polarization resolved second harmonic generation was used to align the $MoSe_2$ and WSe_2 layers to near 0° (*37, 38*), and a bilayer hBN layer was chosen to separate the $MoSe_2$ and WSe_2 layers. The optical signatures of the device are consistent with other R-type heterostructures (*10*). In addition to extending the lifetime of IXs, the bilayer hBN spacer suppresses the moiré potential in the device (*39*). 8 nm thick hBN was used as the top layer, and 22 nm thick bottom hBN was used. The layers were stacked using a polymer based dry transfer method (*40*).

Optical Measurements

Spatial PL measurements were taken by exciting the sample in an optical cryostat with a 76 MHz 120 fs Ti:sapphire laser centered about 720 nm (see Fig. S2B-E for coherence measurements of the laser). PL images were rotated using two dove prisms. The sample's temperature was controlled by an attocube attodry 2100 cryostat. The sample was excited and imaged using an integrated NA= 0.81 objective lens. The hBN region emits PL centered about 1.42 eV (870 nm), and the DC region about 1.34 eV (920 nm) (*10*). 800 nm and 850 nm long pass filters were used to reject the 720 nm laser and monolayer exciton PL. When imaging the hBN separated signal, a 900 nm short pass filter was used to block the direct contact signal. When imaging the direct contact signal, a 900 nm long pass filter was used to reject the hBN separated signal. The PL was magnified and imaged using a 1 m lens and a cooled scientific camera (Andor Newton). Lifetime measurements were taken using an acousto-optic-modulator based pulse picker to increase the repetition period to 3.1 μs, and the IX PL was measured using a spectrometer and a time correlated single photon counting setup (Picoquant).

References and Notes

1. L. V. Keldysh, A. N. Kozlov, Collective properties of excitons in semiconductors. *J. Exp. Theor. Phys.* **27**, 521 (1968).
2. J. M. Kosterlitz, D. J. Thouless, Ordering, metastability and phase transitions in two-dimensional systems. *Journal of Physics C: Solid State Physics* **6**, 1181 (1973).
3. N. P. Wilson, W. Yao, J. Shan, X. Xu, Excitons and emergent quantum phenomena in stacked 2D semiconductors. *Nature* **599**, 383-392 (2021).
4. L. V. Butov, A. Zrenner, G. Abstreiter, G. Böhm, G. Weimann, Condensation of indirect excitons in coupled AlAs/GaAs quantum wells. *Physical Review Letters* **73**, 304-307 (1994).
5. P. Rivera, J. R. Schaibley, A. M. Jones, J. S. Ross, S. Wu, G. Aivazian, P. Klement, K. Seyler, G. Clark, N. J. Ghimire, J. Yan, D. G. Mandrus, W. Yao, X. Xu, Observation of long-lived interlayer excitons in monolayer $MoSe_2$–WSe_2 heterostructures. *Nature Communications* **6**, 6242 (2015).
6. P. Rivera, K. L. Seyler, H. Yu, J. R. Schaibley, J. Yan, D. G. Mandrus, W. Yao, X. Xu, Valley-polarized exciton dynamics in a 2D semiconductor heterostructure. *Science* **351**, 688-691 (2016).
7. L. A. Jauregui, A. Y. Joe, K. Pistunova, D. S. Wild, A. A. High, Y. Zhou, G. Scuri, K. De Greve, A. Sushko, C.-H. Yu, T. Taniguchi, K. Watanabe, D. J. Needleman, M. D. Lukin, H. Park, P. Kim, Electrical control of interlayer exciton dynamics in atomically thin heterostructures. *Science* **366**, 870-875 (2019).
8. K. L. Seyler, P. Rivera, H. Yu, N. P. Wilson, E. L. Ray, D. G. Mandrus, J. Yan, W. Yao, X. Xu, Signatures of moiré-trapped valley excitons in $MoSe_2$/WSe_2 heterobilayers. *Nature* **567**, 66-70 (2019).
9. T. Song, Q.-C. Sun, E. Anderson, C. Wang, J. Qian, T. Taniguchi, K. Watanabe, M. A. McGuire, R. Stöhr, D. Xiao, T. Cao, J. Wrachtrup, X. Xu, Direct visualization of magnetic domains and moiré magnetism in twisted 2D magnets. *Science* **374**, 1140-1144 (2021).
10. F. Mahdikhanysarvejahany, D. N. Shanks, C. Muccianti, B. H. Badada, I. Idi, A. Alfrey, S. Raglow, M. R. Koehler, D. G. Mandrus, T. Taniguchi, K. Watanabe, O. L. A. Monti, H. Yu, B. J. LeRoy, J. R. Schaibley, Temperature dependent moiré trapping of interlayer excitons in MoSe2-WSe2 heterostructures. *npj 2D Materials and Applications* **5**, 67 (2021).
11. H. Liu, J. Wang, S. Chen, Z. Sun, H. Xu, Y. Han, C. Wang, H. Liu, L. Huang, J. Luo, D. Liu, Direct visualization of dark interlayer exciton transport in moiré superlattices. *Nano Letters* **24**, 339-346 (2024).
12. D. N. Shanks, F. Mahdikhanysarvejahany, C. Muccianti, A. Alfrey, M. R. Koehler, D. G. Mandrus, T. Taniguchi, K. Watanabe, H. Yu, B. J. LeRoy, J. R. Schaibley, Nanoscale trapping of interlayer excitons in a 2D semiconductor deterostructure. *Nano Letters* **21**, 5641-5647 (2021).
13. D. N. Shanks, F. Mahdikhanysarvejahany, M. R. Koehler, D. G. Mandrus, T. Taniguchi, K. Watanabe, B. J. LeRoy, J. R. Schaibley, Single-exciton trapping in an electrostatically defined two-dimensional semiconductor quantum dot. *Physical Review B* **106**, L201401 (2022).
14. F. Tagarelli, E. Lopriore, D. Erkensten, R. Perea-Causín, S. Brem, J. Hagel, Z. Sun, G. Pasquale, K. Watanabe, T. Taniguchi, E. Malic, A. Kis, Electrical control of hybrid exciton transport in a van der Waals heterostructure. *Nature Photonics* **17**, 615-621 (2023).

15. D. N. Shanks, F. Mahdikhanysarvejahany, T. G. Stanfill, M. R. Koehler, D. G. Mandrus, T. Taniguchi, K. Watanabe, B. J. LeRoy, J. R. Schaibley, Interlayer exciton diode and transistor. *Nano Letters* **22**, 6599-6605 (2022).
16. L. H. Fowler-Gerace, Z. Zhou, E. A. Szwed, D. J. Choksy, L. V. Butov, Transport and localization of indirect excitons in a van der Waals heterostructure. *Nature Photonics* **18**, 823-828 (2024).
17. L. Ma, P. X. Nguyen, Z. Wang, Y. Zeng, K. Watanabe, T. Taniguchi, A. H. MacDonald, K. F. Mak, J. Shan, Strongly correlated excitonic insulator in atomic double layers. *Nature* **598**, 585-589 (2021).
18. R. Qi, A. Y. Joe, Z. Zhang, Y. Zeng, T. Zheng, Q. Feng, J. Xie, E. Regan, Z. Lu, T. Taniguchi, K. Watanabe, S. Tongay, M. F. Crommie, A. H. MacDonald, F. Wang, Thermodynamic behavior of correlated electron-hole fluids in van der Waals heterostructures. *Nature Communications* **14**, 8264 (2023).
19. M. M. Fogler, L. V. Butov, K. S. Novoselov, High-temperature superfluidity with indirect excitons in van der Waals heterostructures. *Nature Communications* **5**, 4555 (2014).
20. F.-C. Wu, F. Xue, A. H. MacDonald, Theory of two-dimensional spatially indirect equilibrium exciton condensates. *Physical Review B* **92**, 165121 (2015).
21. C. Lagoin, F. Dubin, Key role of the moiré potential for the quasicondensation of interlayer excitons in van der Waals heterostructures. *Physical Review B* **103**, L041406 (2021).
22. B. Remez, N. R. Cooper, Leaky exciton condensates in transition metal dichalcogenide moiré bilayers. *Physical Review Research* **4**, L022042 (2022).
23. Z. Wang, D. A. Rhodes, K. Watanabe, T. Taniguchi, J. C. Hone, J. Shan, K. F. Mak, Evidence of high-temperature exciton condensation in two-dimensional atomic double layers. *Nature* **574**, 76-80 (2019).
24. B. Sun, W. Zhao, T. Palomaki, Z. Fei, E. Runburg, P. Malinowski, X. Huang, J. Cenker, Y.-T. Cui, J.-H. Chu, X. Xu, S. S. Ataei, D. Varsano, M. Palummo, E. Molinari, M. Rontani, D. H. Cobden, Evidence for equilibrium exciton condensation in monolayer WTe_2. *Nature Physics* **18**, 94-99 (2022).
25. L. Sigl, F. Sigger, F. Kronowetter, J. Kiemle, J. Klein, K. Watanabe, T. Taniguchi, J. J. Finley, U. Wurstbauer, A. W. Holleitner, Signatures of a degenerate many-body state of interlayer excitons in a van der Waals heterostack. *Physical Review Research* **2**, 042044 (2020).
26. J. I. A. Li, T. Taniguchi, K. Watanabe, J. Hone, C. R. Dean, Excitonic superfluid phase in double bilayer graphene. *Nature Physics* **13**, 751-755 (2017).
27. E. Y. Paik, L. Zhang, G. W. Burg, R. Gogna, E. Tutuc, H. Deng, Interlayer exciton laser of extended spatial coherence in atomically thin heterostructures. *Nature* **576**, 80-84 (2019).
28. M. Troue, J. Figueiredo, L. Sigl, C. Paspalides, M. Katzer, T. Taniguchi, K. Watanabe, M. Selig, A. Knorr, U. Wurstbauer, A. W. Holleitner, Extended spatial coherence of interlayer excitons in $MoSe_2/WSe_2$ heterobilayers. *Physical Review Letters* **131**, 036902 (2023).
29. M. M. Fogler, S. Yang, A. T. Hammack, L. V. Butov, A. C. Gossard, Effect of spatial resolution on the estimates of the coherence length of excitons in quantum wells. *Physical Review B* **78**, 035411 (2008).
30. A. Filinov, N. V. Prokof'ev, M. Bonitz, Berezinskii-Kosterlitz-Thouless Transition in Two-Dimensional Dipole Systems. *Physical Review Letters* **105**, 070401 (2010).

31. X. Hong, J. Kim, S.-F. Shi, Y. Zhang, C. Jin, Y. Sun, S. Tongay, J. Wu, Y. Zhang, F. Wang, Ultrafast charge transfer in atomically thin MoS_2/WS_2 heterostructures. *Nature Nanotechnology* **9**, 682-686 (2014).
32. C. Jin, E. Y. Ma, O. Karni, E. C. Regan, F. Wang, T. F. Heinz, Ultrafast dynamics in van der Waals heterostructures. *Nature Nanotechnology* **13**, 994-1003 (2018).
33. D. Caputo, D. Ballarini, G. Dagvadorj, C. Sánchez Muñoz, M. De Giorgi, L. Dominici, K. West, L. N. Pfeiffer, G. Gigli, F. P. Laussy, Marzena H. Szymańska, D. Sanvitto, Topological order and thermal equilibrium in polariton condensates. *Nature Materials* **17**, 145-151 (2018).
34. J. R. Schaibley, H. Yu, G. Clark, P. Rivera, J. S. Ross, K. L. Seyler, W. Yao, X. Xu, Valleytronics in 2D materials. *Nature Reviews Materials* **1**, 16055 (2016).
35. E. Schwartz, B. Li, A. A. Kovalev, Superfluid spin transistor. *Physical Review Research* **4**, 023236 (2022).
36. L. Amico, D. Aghamalyan, F. Auksztol, H. Crepaz, R. Dumke, L. C. Kwek, Superfluid qubit systems with ring shaped optical lattices. *Scientific Reports* **4**, 4298 (2014).
37. L. M. Malard, T. V. Alencar, A. P. M. Barboza, K. F. Mak, A. M. de Paula, Observation of intense second harmonic generation from MoS_2 atomic crystals. *Physical Review B* **87**, 201401 (2013).
38. N. Kumar, S. Najmaei, Q. Cui, F. Ceballos, P. M. Ajayan, J. Lou, H. Zhao, Second harmonic microscopy of monolayer MoS_2. *Physical Review B* **87**, 161403 (2013).
39. F. Mahdikhanysarvejahany, D. N. Shanks, M. Klein, Q. Wang, M. R. Koehler, D. G. Mandrus, T. Taniguchi, K. Watanabe, O. L. A. Monti, B. J. LeRoy, J. R. Schaibley, Localized interlayer excitons in MoSe2–WSe2 heterostructures without a moiré potential. *Nature Communications* **13**, 5354 (2022).
40. P. J. Zomer, M. H. D. Guimarães, J. C. Brant, N. Tombros, B. J. van Wees, Fast pick up technique for high quality heterostructures of bilayer graphene and hexagonal boron nitride. *Applied Physics Letters* **105**, (2014).
41. G. Moody, C. Kavir Dass, K. Hao, C.-H. Chen, L.-J. Li, A. Singh, K. Tran, G. Clark, X. Xu, G. Berghäuser, E. Malic, A. Knorr, X. Li, Intrinsic homogeneous linewidth and broadening mechanisms of excitons in monolayer transition metal dichalcogenides. *Nature Communications* **6**, 8315 (2015).

Acknowledgments:

We acknowledge useful discussions with Brian Anderson.

Funding:

National Science Foundation grant DMR-2003583 (JRS, BJL)
National Science Foundation grant ECCS-2054572 (JRS, BJL)
Air Force Office of Scientific Research grant FA9550-20-1-0217 (JRS)
Air Force Office of Scientific Research grant FA9550-21-1-0219 (JRS)
Air Force Office of Scientific Research grant FA9550-22-1-0312 (JRS)
Army Research Office grant W911NF-18-1-0420 (BJL)
Army Research Office grant W911-NF-20-1-0215 (BJL)
Gordon and Betty Moore Foundation's EPiQS Initiative grant GBMF9069 (DGM)
JSPS KAKENHI grant 21H05233 (KW, TT)
JSPS KAKENHI grant 23H02052 (KW, TT)
World Premier International Research Center Initiative (WPI), MEXT, Japan (KW, TT)
NKRDPC grant 2022YFA1405304 (QZ)
NSFC grant 12004118 (QZ)

Author Contributions:

Conceptualization: JRS, BJL, FM, AR
Methodology: JC, FM, JRS, BJL, QZ
Investigation: JC, FM, AR
Visualization: JC, BJL, AR
Funding acquisition: BJL, JRS, QZ
Project administration: JRS, BJL, JC, FM
Supervision: JRS, BJL, FM, JC
Writing – original draft: JC, JRS, BJL
Writing – review & editing: JC, JRS, BJL, FM, QZ, KW, TT, DNS, AR
Resources: MRK, DGM, TT, KW, DGM

Competing Interests:

The authors declare no competing interests.

Data availability:

All data needed to evaluate the conclusions of the paper are present in the paper and/or the Supplementary Materials. Data sets can be found at: 10.25422/azu.data.27266079.

Supplementary Materials:

Materials and Methods
Supplementary Text
Figs. S1 to S10
Reference (41)

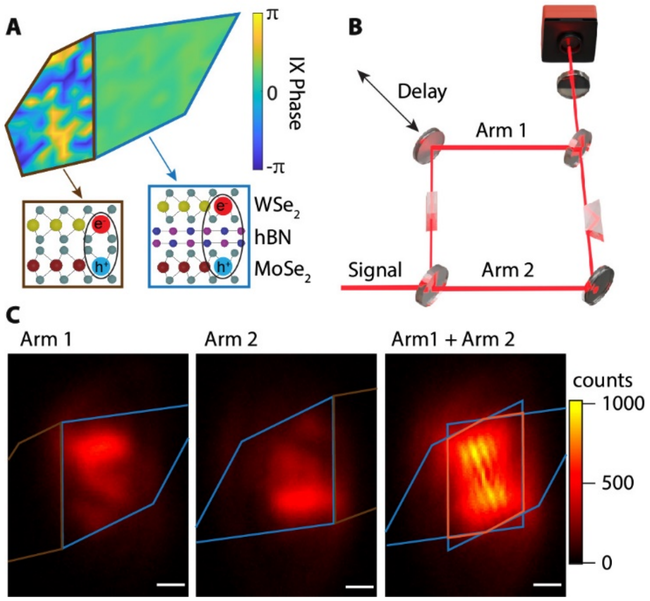

Fig. 1: Long range spatial coherence from interlayer excitons (IXs). (**A**) Top and side views of 2D heterostructure: monolayer $MoSe_2$ (yellow and green), WSe_2 (red and green), and bilayer hBN (pink and blue). The direct contact side (DC region) is outlined in brown, and the hBN separated side (hBN region) in blue. The color depicts IX quantum phase. As IX density is increased the IXs in the hBN region take on a near uniform phase as they enter a superfluid state. The DC region always shows highly non uniform IX phase. (**B**) A depiction of the experimental set up. IX PL signal was sent through two arms of a Mach-Zehnder interferometer. Arm 1 and Arm 2 images were inverted using two dove prisms. A delay stage was used to control the time delay of the two arms. The PL and interferogram images were measured with a cooled camera. (**C**) PL signal and interferogram from the hBN separated region when excited at 150 µW at 1.6 K. The hBN region and rotated hBN regions are outlined in blue, the overlap region between the two arms is outlined in orange. White scale bars represent 1 µm.

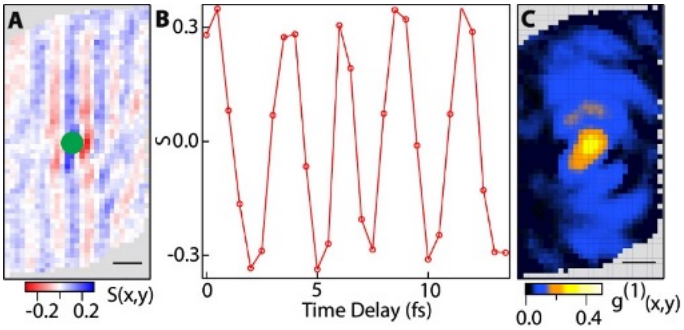

Fig. 2: Extracting the spatial coherence function $g^{(1)}(\vec{r})$ from the interferograms. (**A**) Coherence fringes, S, resolved over the overlap region outlined in Fig. 1C by subtracting the Arm 1 and Arm 2 contributions from the interference pattern shown in Fig. 1C and normalizing. (**B**) Intensity oscillation at the location of the green pixel when scanning the delay stage in 0.5 fs steps over 13 fs. (**C**) Spatially resolved first order coherence $g^{(1)}(\vec{r})$ measured by taking the amplitude of the oscillation shown in b for all pixels. The area outside the overlap region is shown in gray. Scale bars represent 500 nm.

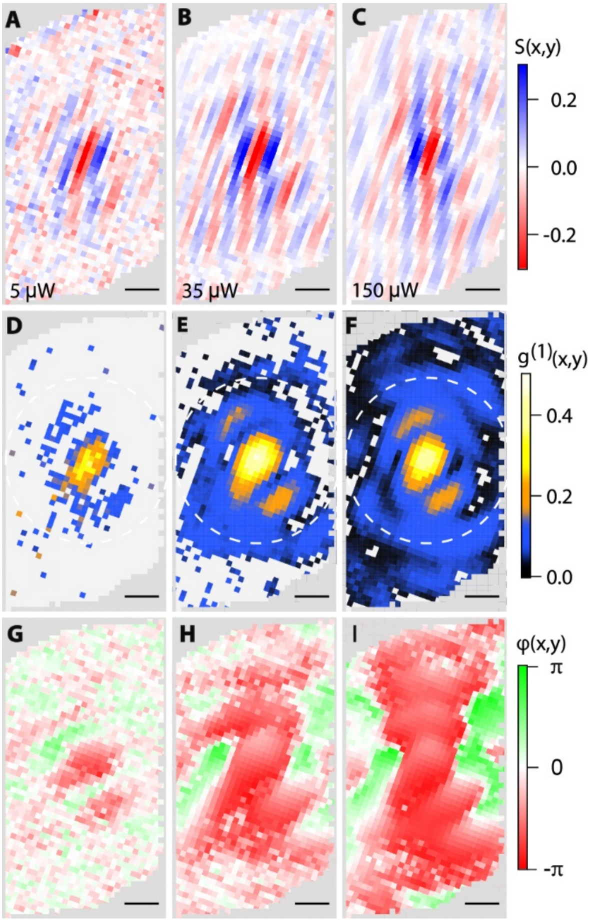

Fig. 3: Power dependence of the spatial coherence 15 K. (**A-C**) Power dependent, averaged fringe contrast from the hBN separated emission. As the power (IX density) is increased, fringes spread across the length of the entire overlap region**.** (**D-F**) Power dependent spatial coherence of IX emission in the hBN separated device. A bright central spot is observed at all powers with a diameter of ~0.5 μm, the resolution of the collection objective. At higher powers, longer range spatial coherence is observed further away from the central spot. The white dashed circle shows the ring radially averaged over to produce the phase diagram in Fig. 4E. (**G-I**) Power dependent phase resolved for the hBN separated region. As coherence spreads, nearly uniform phase is observed across the entire overlap region.

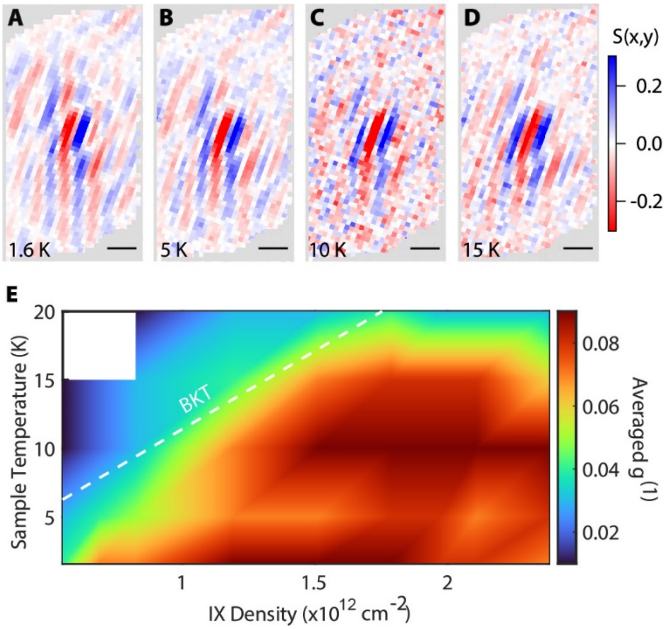

Fig. 4: IX transition to a superfluid phase. (**A-D**) Fringe contrast within the overlap region for four different sample temperatures at 10 μW excitation. As temperature is increased long range coherence decreases. (**E**) Phase diagram resolved by radially averaging over the ring shown in Fig. 3D-F as a function of IX density and sample temperature. As the temperature reaches 20 K, the signal to noise becomes too low for low excitation powers, so the two lowest powers are excluded from analysis. The white line shows the theoretically predicted BKT line from reference (*19*).

Supplementary Text

S1. Measurement of $g^{(1)}$ Amplitude

To measure the amplitude of the spatial coherence function, interferograms were measured over a series of time delays using 0.5 fs steps. Then for each spatial location in the interferogram, the interference contrast signal was determined. Taking a temporal Fourier transform gives a signal with a component at $\omega = \frac{\lambda}{c}$. The amplitude of this component gives the amplitude of $g^{(1)}$. For spatial locations where the amplitude of $g^{(1)}$ was less than 4 times the noise floor from the Fourier transform, the value was set to 0. Due to a crack in the hBN region of the sample, the region of non-zero (blue) coherence observed in Fig. 2C is slightly narrower than the overlap region. For further analysis of the coherence signal only this non-zero region was utilized.

S2. Measurement of $g^{(1)}$ Phase

From the interferograms it is possible to extract phase information of the spatial coherence function. This is done using the following algorithm. First, we can write the interference contrast in complex exponential form,

$$S(\vec{r}, t) = g(\vec{r})\mathrm{e}^{2\pi \mathrm{i}\vec{q}\cdot\vec{r}} + g^{*}(\vec{r})\mathrm{e}^{-2\pi \mathrm{i}\vec{q}\cdot\vec{r}}.$$

where $g(\vec{r}, t) = \frac{1}{2} g^{(1)}(\vec{r})\mathrm{e}^{\mathrm{i}(\frac{2\pi c}{\lambda}\Delta \mathrm{t} + \phi(\vec{r}))}$ and $\vec{q}$ is the vector associated with the tilt between the two arms of the interferometer which causes the spatial interference fringes. At a given time delay, the spatial Fourier transform of the interference contrast can be written as

$$\tilde{S}(\vec{k}, t) = \tilde{g}(\vec{k} - \vec{q}, t) + \widetilde{g^{*}}(\vec{k} + \vec{q}, t).$$

where $\tilde{g}$ is the Fourier transform of g. As the interference contrast is real, we can take only one of the two components of $\tilde{S}(\vec{k}, t)$ without the loss of any information. This component is then shifted in frequency space by an amount $\vec{q}$ to obtain $\tilde{g}(\vec{k}, t)$. Lastly, we take the inverse Fourier transform to obtain the phase information as

$$\phi(\vec{r}, t) + \frac{2\pi c}{\lambda}\Delta\mathrm{t} = \tan^{-1}\frac{\Im\, g(\vec{r}, t)}{\Re\, g(\vec{r}, t)}.$$

As the time delay is changed between each image, there is an overall phase shift of the signal due to the $\frac{2\pi c}{\lambda}\Delta\mathrm{t}$ term. Therefore, we set the center pixel at each time delay to a fixed phase value and measure changes in phase with respect to this value. After setting the center pixel to a fixed phase, a total of 27 fringe contrast images are averaged over a time delay of 13 fs to obtain the images in Fig. 3A-C and Fig. 4A-D. The measured phase (Fig. 3G-I) is determined by averaging over the phase at each time delay.

S3. IX Density Calculation

The number of intralayer excitons and IXs can be found from the following rate equations,

$$\frac{\partial N_m}{\partial t} = \frac{\alpha\, P}{\hbar\omega} - \gamma_m N_m - \gamma_t N_m,$$

$$\frac{\partial N_{IX}}{\partial t} = \gamma_t N_m - \gamma_{IX} N_{IX},$$

where N_m is the number of excitons generated in the $MoSe_2$ layer, N_{IX} is the number of IXs in the heterostructure, γ_{IX} is the IX decay rate, γ_m is the $MoSe_2$ intralayer exciton decay rate, α is the absorption coefficient, P is the excitation power, $\hbar\omega$ is the laser photon energy, and γ_t is the $MoSe_2$-WSe_2 hole transfer rate. In the steady state, there is no time dependence in the number of excitons giving:

$$N_m = \frac{\alpha\, P}{(\gamma_m + \gamma_t)\hbar\omega},$$

$$N_{IX} = \frac{\gamma_t \alpha\, P}{\gamma_{IX}(\gamma_m + \gamma_t)\hbar\omega}.$$

To estimate the IX density from the PL measurements, the signal per unit time, calculated by summing the background subtracted PL emission on the CCD for the hBN separated and DC regions separately, can be written as:

$$I_{DC} = \frac{\beta N_{DC}}{\tau_{DC}},$$

$$I_{hBN} = \frac{\beta N_{hBN}}{\tau_{hBN}}.$$

where N_{DC} and N_{hBN} are the number of IXs in the DC and hBN regions respectively, τ_{DC} and τ_{hBN} are the IX lifetimes in the DC and hBN regions respectively, and β is a constant that accounts for loss through collection efficiency, reflection efficiency, and transmission efficiency through all optics.

At low excitation power the lifetimes of IXs in the hBN and DC regions are known (Fig. S2). γ_{IX} is found through lifetime measurements to be (40 ns)$^{-1}$ in the DC region, γ_m is estimated to be (0.5 ps)$^{-1}$ (*31*), and γ_t is taken to be (0.05 ps)$^{-1}$ (*41*) which means that N_{DC} can be simplified to:

$$N_{DC} \approx \frac{\alpha\, P\tau_{DC}}{\hbar\omega}.$$

which gives a value of β based on all measured quantities. This value of β is then utilized to calculate the number of IXs in the hBN region based on the strength of the PL signal and the measured lifetime. Using this method, the exact values of the $MoSe_2$-WSe_2 hole transfer rate and intralayer exciton decay rate do not need to be known to determine the number of IXs in the hBN region. The densities can then be calculated by dividing the number of IXs by the area which is ~4x4 μm for both the DC and hBN regions. As the excitation power is increased the density of excitons is scaled by the increase in PL intensity in both regions. These density estimates assume a constant IX lifetime with power and temperature. Due to the long IX lifetimes of the hBN and DC regions relative to the laser repetition period of 13.2 ns, power and temperature dependent lifetimes cannot be measured under the conditions used in this experiment. However, any consequential change in lifetime should be detectable in the IX emission intensity. Fig. S6A shows minimal variation in PL intensity with temperature and an increase in emission intensity with excitation power.

S4. Analysis of Interferometer Contrast and Exposure Time

The longer exposure time (120 s) required to measure the emission from the hBN separated region of the device compared to the DC region (30 s) reduces the interference contrast and the value of $g^{(1)}$, which is due to instability of our interferometer. We can demonstrate this effect using a narrow linewidth continuous wave (CW) laser, which is a highly coherent source and should have interference contrast between 1 and -1. Figure R4 shows the interference contrast of a CW laser emitting 720 nm light taken at 30 s and 120 s exposure times. There is a clear decrease in contrast when the fringes are averaged over longer exposure times. This decrease can be quantified by fitting to the fringes with a sine wave and extracting the $g^{(1)}$ value. We find that the reported $g^{(1)}$ value decreases by 30 percent. As shown in Fig. 2 and Fig. S3, the central $g^{(1)}$ in the hBN region reaches a maximum of 0.52 and in the DC region it reaches a maximum of 0.53. We take the ratio $g^{(1)}_{\text{max}}/g^{(1)}_{\text{laser}}$ for both the hBN and DC regions to see that the hBN region reaches 85.2% of the maximum value for its exposure time, while the DC region reaches 60.9% of the maximum value at that exposure time. Once correcting for the loss of contrast due to exposure time, the hBN region shows higher coherence than the DC region.

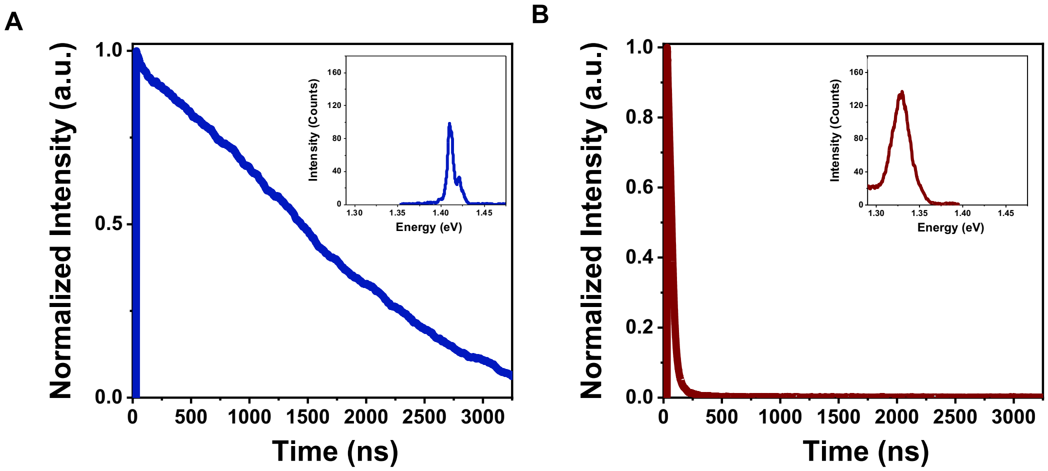

Fig. S1. IX lifetime measurements in hBN and DC regions. (**A**) The blue curve shows PL intensity as a function of time for the hBN region showing hBN IX lifetime to be ~1900 ns. (**B**) The maroon curve shows the PL intensity as a function of time for DC region showing DC IX lifetime to be ~42 ns. Both measurements were taken with 0.63 µW average excitation power. Insets show the PL spectrum of each region.

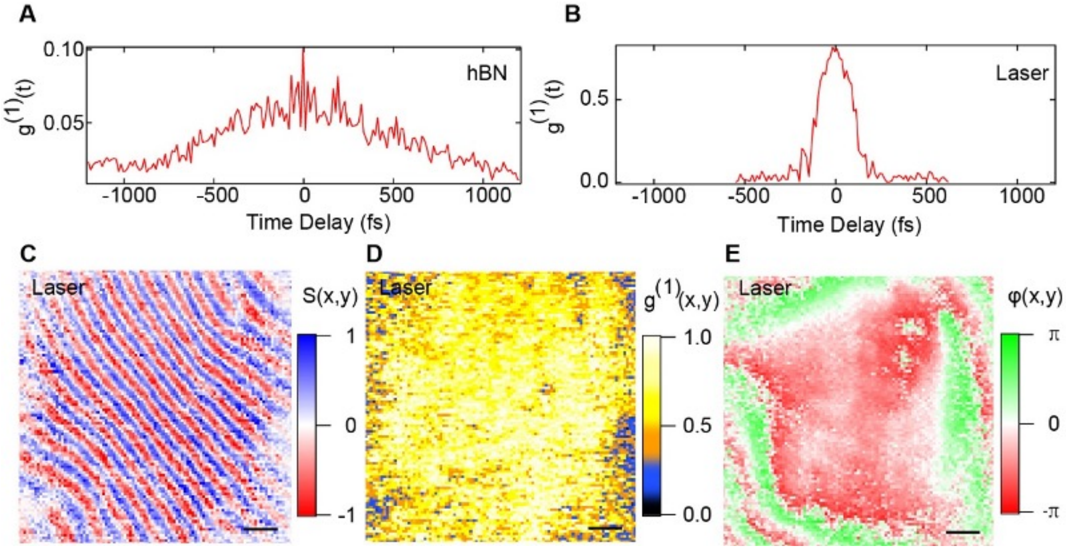

Fig. S2. Temporal coherence of hBN IX and coherence of laser. (**A**) Temporally resolved first order coherence function for the hBN region. $g^{(1)}(t)$ is resolved by taking a time scan similar to that described in Fig. 2 over 2600 fs with 13 fs steps. For each time step the amplitude of $g^{(1)}$ at the center of the image is determined. (**B**) $g^{(1)}(t)$ resolved for the laser showing a narrower temporal coherence length than the hBN separated region. (**C-E**) Fringe contrast, spatial coherence function, and phase for the laser showing the expected results for a coherent source. Scale bars represent 500nm.

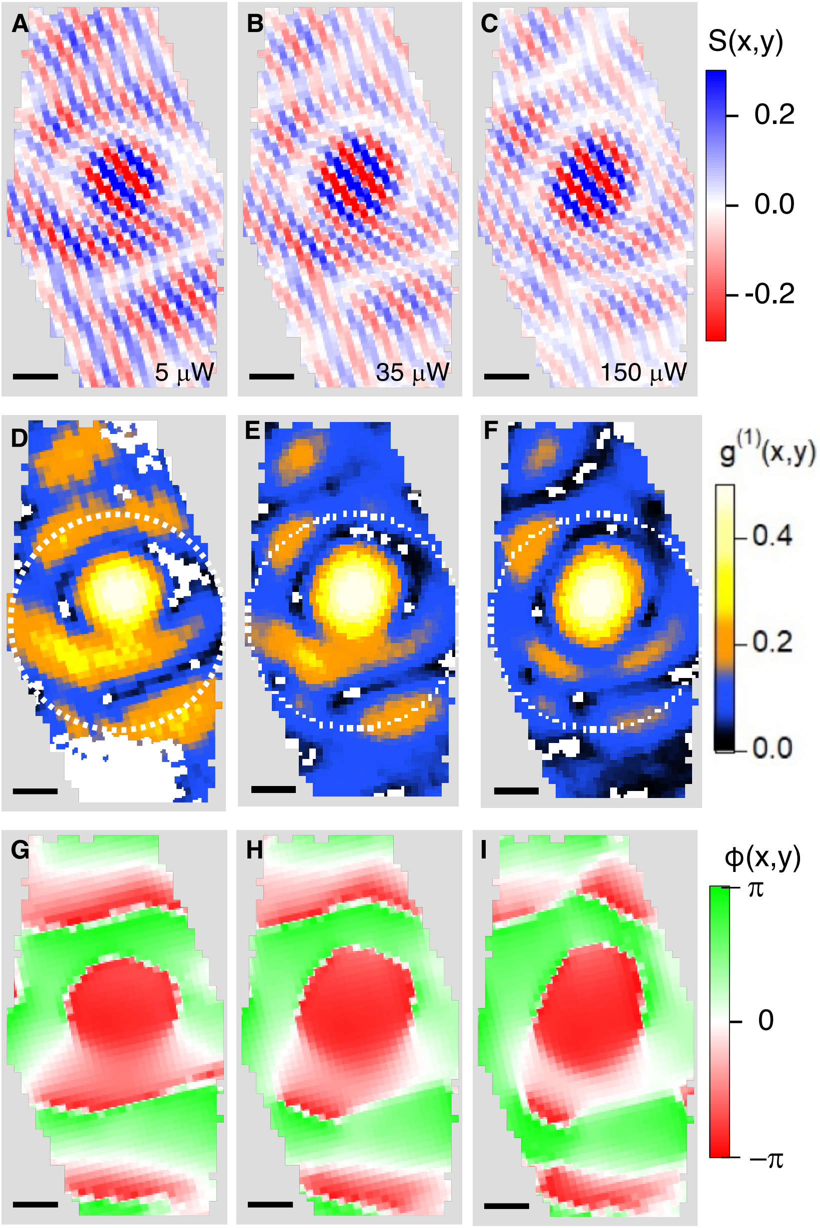

Fig. S3. Fringe contrast, spatial coherence, and phase for DC PL. (**A-C**) Fringe contrast at different excitation powers measured for the DC region of the device showing multiple discontinuities in the interference fringes over the overlap region. (**D-F**) Spatially resolved first order coherence function for the DC region showing multiple maxima and minima resulting from the discontinuities shown in A-C. (**G-I**) Fringe phase for the DC region showing non-uniform phase throughout the overlap region.

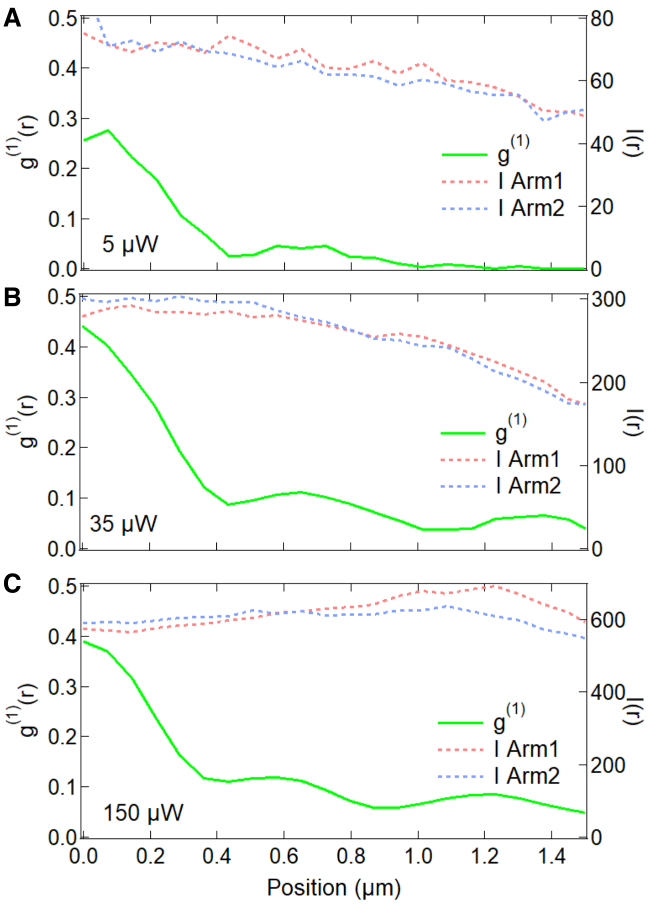

Fig S4. Radially averaged $g^{(1)}(\vec{r})$ and PL emission from hBN region at 5, 35, and 150 μW. (**A-C**) The green curves are the radially averaged first order spatial coherence function as a function of power (left axis). The dashed red and blue lines (right axis) show the radially averaged PL intensities for each arm (Arm 1 and Arm 2) of the interferometer which are nearly constant.

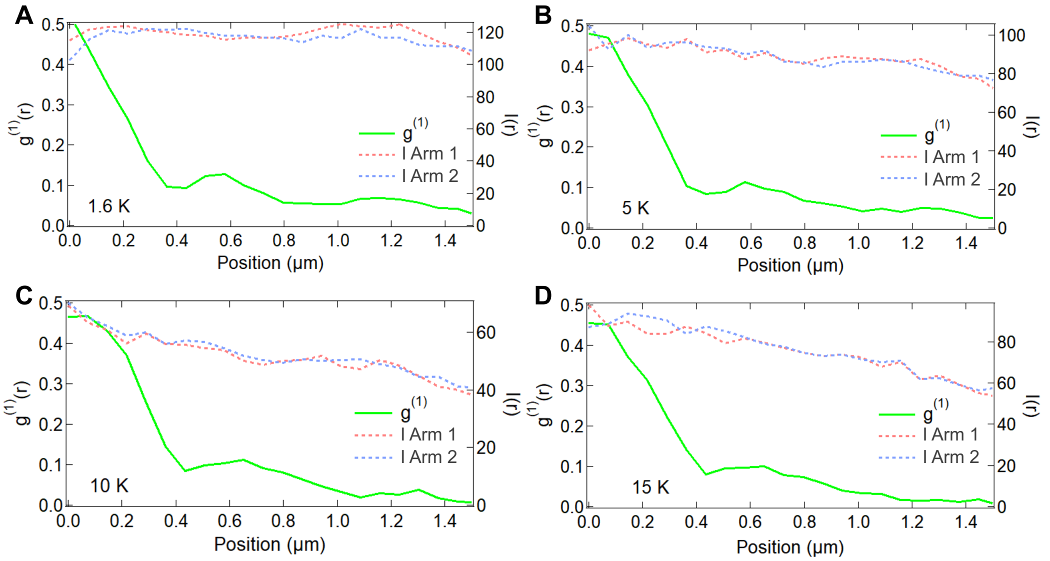

Fig. S5. Temperature dependence of radially averaged $g^{(1)}(\vec{r})$ and PL emission from hBN at 10 µW excitation. (**A-D**) The green curves show the radially averaged first order spatial coherence function for four different temperatures (left axis). The dashed red and blue lines (right axis) show the radially averaged PL intensities for each arm (Arm 1 and Arm 2) of the interferometer which are nearly constant.

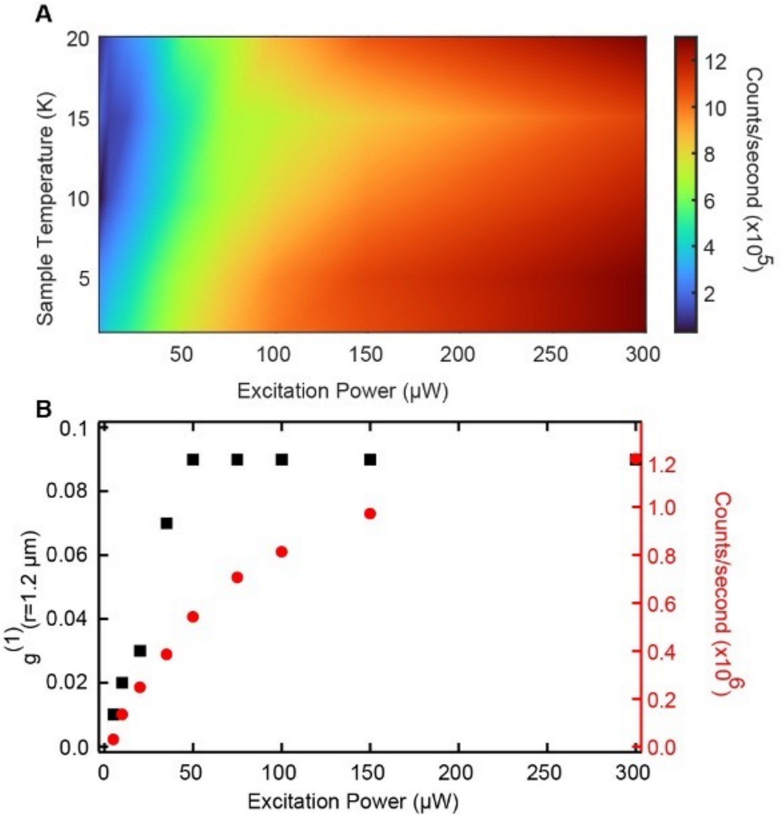

Fig. S6. Analysis of PL intensity power and temperature dependence. (**A**) Counts/second from the hBN separated IX emission integrated over the entire CCD as a function of excitation power and sample temperature showing minimal variation with temperature and increase with power. (**B**) Excitation power dependent radially averaged $g^{(1)}$ at r = 1.2 μm showing a sharp increase at low powers and constant value at high powers while emission intensity saturates at high power but continues to increase.

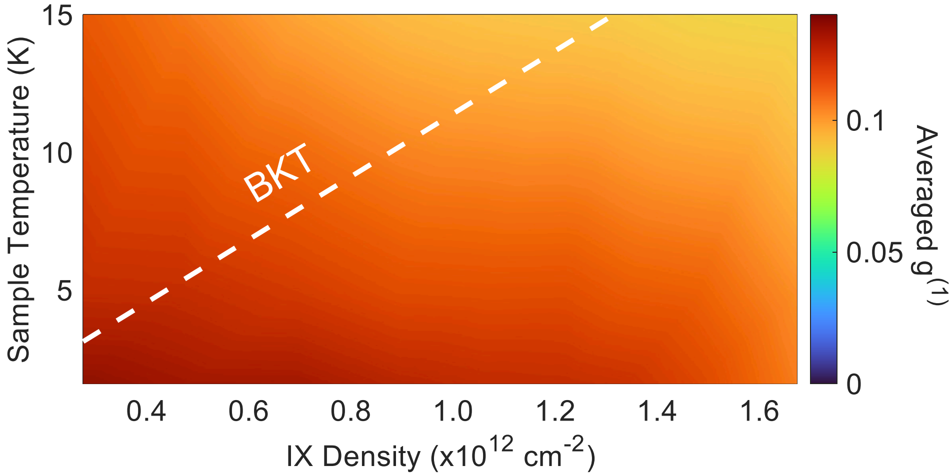

Fig. S7. Phase diagram for the DC region. The phase diagram for the DC region resolved by radially averaging over the white dashed line shown in Extended Data Fig. 3D-F. No transition is observed. The white line shows the theoretical BKT line from reference (*19*).

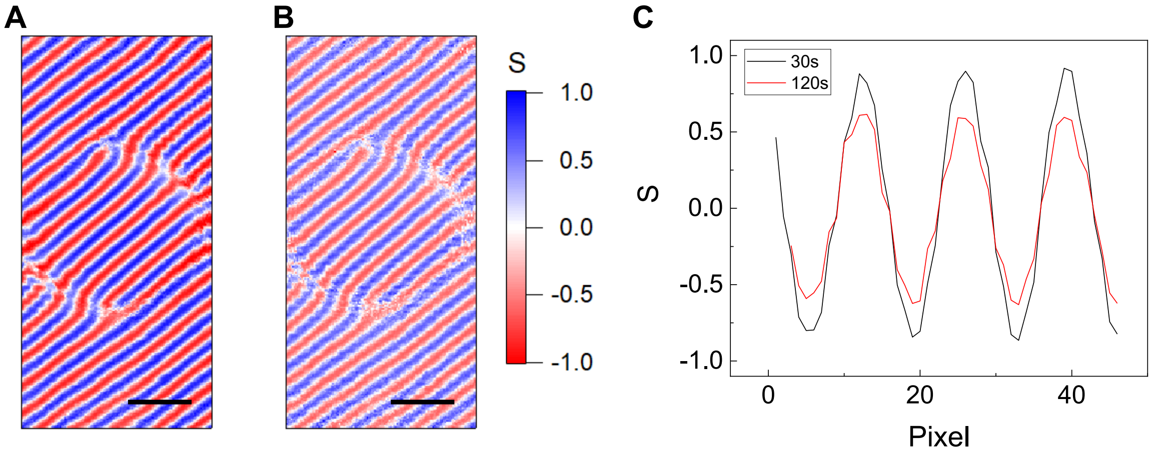

Fig. S8. Comparison of fringe contrast at different exposure times. Laser fringe interference contrast taken at (**A**) 30 s exposure time and (**B**) 120 s exposure time. (**C**) Line cuts taken perpendicular to the fringes shown in A and B.

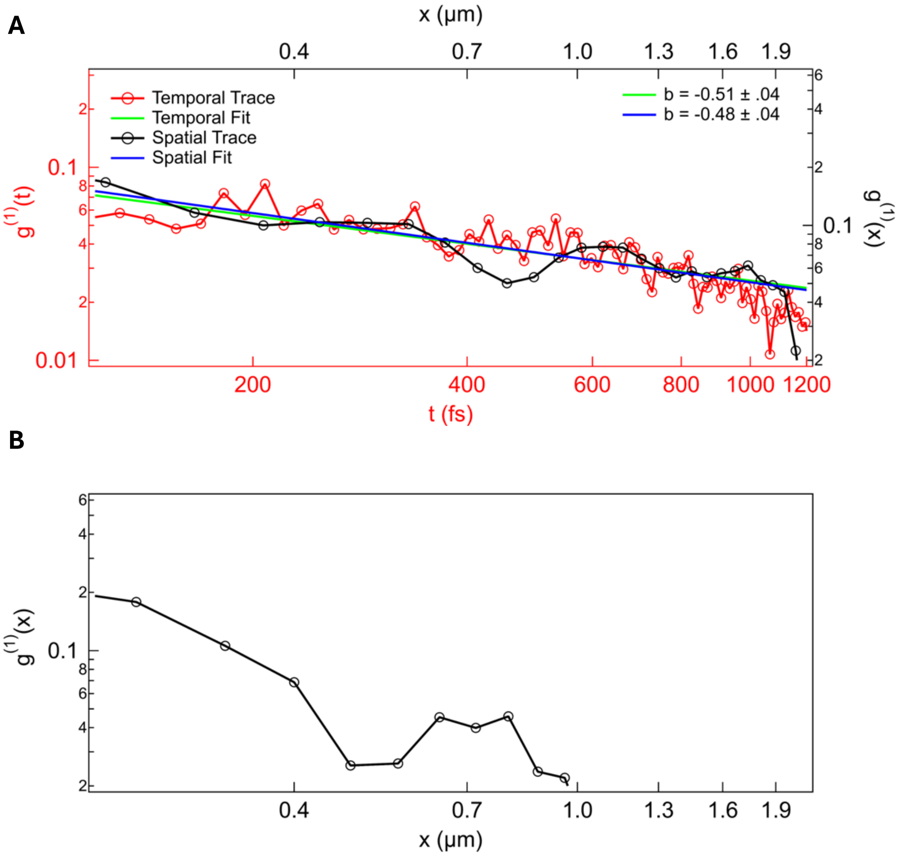

Fig. S9. **Comparison of temporal and spatial decay. (A)** Temporal coherence trace taken at 200 µW and spatial coherence trace taken at 150 µW with a power law fit of the form $g^1(u) = Au^b$, where u is either time or position, showing comparable exponents. (**B)** Spatial coherence trace at 15 K and 5 µW showing notably faster decay than the trace shown in A.

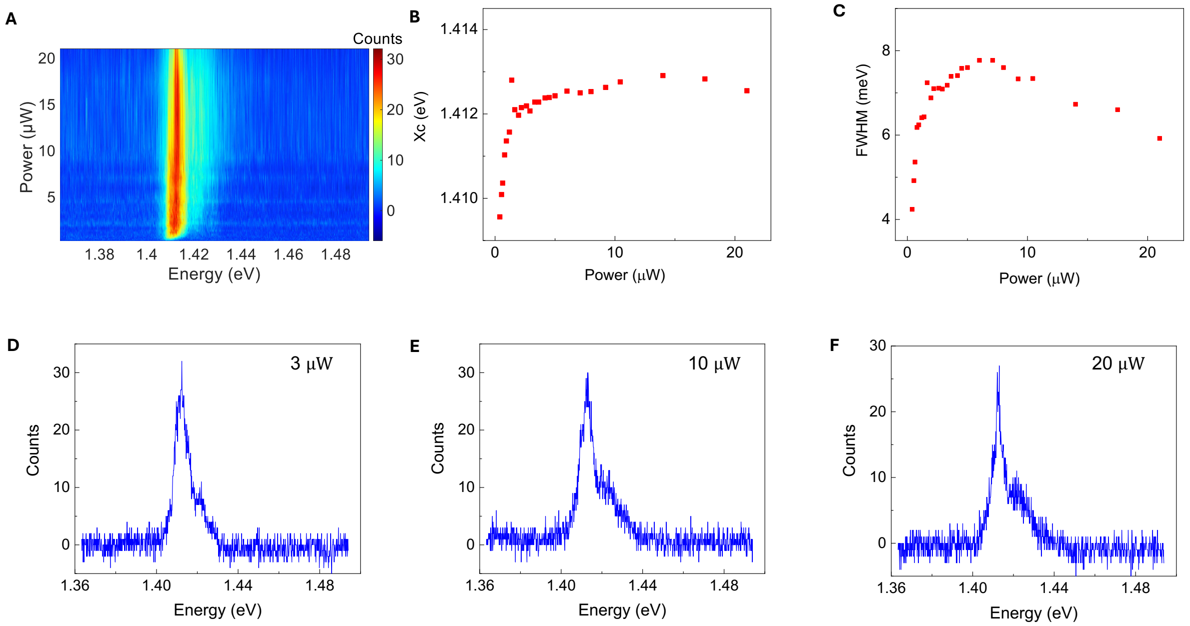

Fig. S10. Analysis of PL spectra as a function of excitation power. (A) Excitation power dependent PL emission for the hBN separated region at 1.6 K showing notable narrowing at higher powers. **(B)** Power dependent center energy showing an initial increase with excitation power. **(C)** Power dependent PL linewidth showing an initial increase followed by a decrease. **(D-F)** PL emission taken at 3 μW (D), 10 μW (E), and 20 μW showing two different peak structures at low and high densities.